New insights into the failure mechanisms of horizontal plate anchors in clay during pull-out

Jalilvand, Soroosh; Gavin, Kenneth; Sivakumar, Vinayagamoothy; Gilbert, Robert B.; Bradshaw, Aaron

DOI
10.1680/jgeot.18.P.283

Publication date
2021

Document Version
Final published version

Published in
Geotechnique

New insights into the failure mechanisms of horizontal plate anchors in clay during pull-out

SOROOSH JALILVAND*, KENNETH GAVIN†, VINAYAGAMOOTHY SIVAKUMAR‡, ROBERT B. GILBERT§ and AARON BRADSHAW‖

Offshore wind developments are moving towards deep-water regions where energy is abundant, visual impact is minimised and the larger turbine sizes can make the energy production more cost-effective. One of the key challenges facing the industry is the development of reliable substructures. While fixed foundation systems are widely used for shallow-water (<60 m) developments, permanent anchors are seen as one of the most viable mooring solutions for floating structures in deep water. In the current study, the pull-out behaviour of square plate anchors in clay was investigated using large-displacement finite-element analysis. The anchor capacity and failure mechanism were considered for a range of embedment ratios and undrained shear strengths. Three distinct modes of anchor failure identified in previous studies were examined through the analysis of four descriptors including: the pull-out capacity of the anchor, the pull-out displacement required to mobilise this capacity, the energy absorbed by the anchor during pull-out and the variation of the pull-out capacity with respect to a normalised overburden pressure. The findings of the study are presented in the form of a series of charts that can aid design through understanding of the factors controlling the development of anchor failure modes, in addition to identifying the transition point between different failure mechanisms.

KEYWORDS: anchors & anchorages; finite-element modelling; offshore engineering

INTRODUCTION

Floating platforms are considered to be the most viable foundation solution for offshore renewable developments in water depths of greater than 60 m (Schwartz *et al*., 2010). In the offshore oil and gas sector the use of floating platforms has resulted in the development of a range of anchor systems. These include drag embedded (Aubeny & Chi, 2010), suction embedded (Wong *et al*., 2012) and dynamically installed anchors (Blake *et al*., 2015). These anchors are reliant, to various extents, on the bearing area of their planar parts to develop their ultimate pull-out capacity. This reliance is realised either through a complete planar body shape as in vertically loaded anchors (Murff *et al*., 2005), or in the form of planar features such as fins on Omni-Max anchors (Shelton, 2007).

Significant investigations in the form of laboratory, field and numerical studies have been undertaken to improve the understanding of plate anchor behaviour in fine deposits. These studies reveal that the pull-out capacity of anchors in clay is dependent on a combination of parameters including the anchor's embedment depth, the overburden ratio (i.e. the ratio of overburden pressure to undrained shear strength) and the shape of the plate anchor (Das, 1980; Merifield *et al*., 2003; Singh & Ramaswamy, 2008; Wang *et al*., 2010; Liu *et al*., 2013; Gerkus, 2016).

Based on lower-bound limit analysis, Merifield *et al*. (2003) proposed the uplift capacity factor N_c of a plate anchor can be derived from a linear superposition of the corresponding uplift capacity in weightless soil, N_{c0} and the overburden ratio, which in its general form can be described using equation (1)

$$N_c = N_{c0} + m_s \frac{\gamma' H}{s_u} \leq N_{cmax} \quad (1)$$

where $m_s = (N_c - N_{c0})/(\gamma' H/s_u)$ is the secant slope of pull-out capacity curve at a given embedment ratio (assumed as unity according to Merifield *et al*. (2003)); γ' is the buoyant unit weight of soil; H is the embedded depth of the anchor; s_u is the undrained shear strength of the soil; and N_{cmax} is the maximum pull-out capacity. Merifield *et al*. (2003) highlighted that the bilinear shape of the pull-out capacity phenomenon is associated with two dominant anchor failure mechanisms, namely: (*a*) a shallow failure mode, where the failure mechanism reaches the soil surface, and (*b*) a deep failure mode, where the failure mechanism is localised around the anchor. The local slope of the pull-out capacity curve, $m_t = \partial N_c/\partial(\gamma' H/s_u)$ was derived as unity under a shallow failure mechanism and was shown to approach zero under deep failure mode (Merifield *et al*., 2003). For each embedment depth a critical overburden ratio was also identified that marks the transition between shallow and deep failure mechanisms (Merifield *et al*., 2003; Song *et al*., 2008; Wang *et al*., 2010). Recent studies carried out using large-displacement finite-element analyses (Chen *et al*., 2013; Tho *et al*., 2013) revealed that deeply embedded anchors with low overburden ratios can develop a third failure mode referred to as 'the intermediate failure mechanism', which often occurs when the deep (also referred to as full-flow) mechanism cannot develop fully.

Manuscript received 25 October 2018; revised manuscript accepted 17 August 2020.
Discussion on this paper is welcomed by the editor.
* Formerly of the School of Civil Engineering, University College Dublin, Ireland; now Gavin and Doherty Geosolutions, Dublin, Ireland.
† Faculty of Civil Engineering and Geosciences, TU Delft, the Netherlands (Orcid:0000-0002-0741-1115).
‡ School of Natural and Built Environment, Queen's University Belfast, Northern Ireland, UK.
§ Department of Civil, Architectural and Environmental Engineering, University of Texas at Austin, TX, USA.
‖ Department of Civil & Environmental Engineering, University of Rhode Island, RI, USA.

While considerable effort has been directed toward acquiring quantitative understanding of plate anchor capacity in clay, the description of various anchor failure modes has been mainly performed qualitatively through the analysis of cumulative plastic strains (Gilbert *et al.*, 2009; Yang *et al.*, 2010), shear strain increments (Hu *et al.*, 2011), displacement increments (O'Neill *et al.*, 2003; Yu *et al.*, 2009; Wang *et al.*, 2010), or velocity field data (Merifield *et al.*, 2005; Chen *et al.*, 2013; Fahmy *et al.*, 2013) in the vicinity of the anchor. Although these approaches have led to a valuable understanding of the behaviour of plate anchors, they do not provide a complete insight into the transition of the various failure modes. Furthermore, while pull-out capacity has been characterised by many researchers as a function of embedment depth and overburden ratio, the impact of pull-out displacement on the mobilised uplift capacity has not been investigated in detail.

In the current study large-displacement finite-element analyses were performed to investigate the pull-out capacity of embedded anchors in clay. As a first step, the trends in the variation of anchor capacity with embedment depth and overburden ratio were investigated in order to ensure a consistency with the previously published investigations. This was then followed by an assessment of the pull-out displacement on the evolution of anchor capacity. A link between the failure mode and displacement required to reach the peak capacity suggests that the absorbed energy of the anchor during pull-out could provide an indication of the anchor failure mechanism. As a final step, correlation between the local slope of the capacity curve and the corresponding anchor failure response is examined to provide further insight into different failure mechanisms and their transition. A series of design charts are also presented showing the variation in uplift capacity as a result of change in pull-out displacement, embedment depth and overburden ratio.

METHODOLOGY

In this study the responses of buried anchors were investigated using large-deformation finite-element analysis. Such modelling poses challenges in relation to mesh distortion and numerical instability. Two well-established methods proposed to address these issues include arbitrary Lagrangian–Eulerian (ALE) and coupled Eulerian–Lagrangian (CEL) techniques. The ALE technique addresses problems associated with the mesh distortion using successive re-meshing that allows for transformation of field variables such as displacement and stresses from distorted mesh to a new distortion-free mesh configuration. The CEL method is another effective approach to address large-deformation phenomena. The soil in the CEL technique is defined as an Eulerian material and the plate is defined as a Lagrangian material. In the Lagrangian zone, the mesh and the material always coincide. In the Eulerian region, the material can flow from one element to another. By coupling the two concepts, the CEL technique allows for modelling large-deformation soil–structure interactions without the need to deal with issues such as the mesh distortion that is often encountered in conventional finite-element analysis (Qiu *et al.*, 2011; Wang *et al.*, 2015).

The CEL technique has been used to provide an insight for a number of soil–structure interaction applications such as: pile installation (Ko *et al.*, 2016; Pucker & Grabe, 2012), cone penetration and T-bar installation (Qiu *et al.*, 2011, Tolooiyan & Gavin, 2011; Wang *et al.*, 2015), spud can installation (Fallah *et al.*, 2015; Hu *et al.*, 2014, 2015; Tho *et al.*, 2012). In addition, CEL has also been used to study the stability of partially embedded offshore pipelines (Dutta *et al.*, 2015), and the installation of drag anchors through detailed mooring line simulation (Zhao & Liu, 2016).

In the current study, the CEL technique in Abaqus/Explicit was employed to explore the role of large-deformation phenomena (such as gap formation and closure) in the overall pull-out behaviour of a square plate anchor. The Tresca criterion was adopted to model the elastic–perfectly plastic behaviour of clay with a uniform undrained shear strength, s_u. The ratio of the Young's modulus E and the undrained shear strength (E/s_u) was assumed as 500 and a Poisson's ratio ν was taken as 0·495 (i.e. under undrained conditions). A smooth interface was also considered between the plate and its surrounding soil. In total 129 model predictions were carried out on a square plate anchor of width, $B = 1$ m. The variables considered were plate depth, H, which varied from 0·65 m to 9·04 m ($H/B = 0{\cdot}65$ to 9·04), effective unit weight, γ', that was assumed as 7 kN/m^3 (representing typical soft marine deposits) and zero for weightless soil, and undrained strength, which varied from 0·42 kN/m^2 to 60 kN/m^2. The domain width was considered as $20 \times B$, while the distance between the base of the domain and the plate anchor was assumed as $10 \times B$. The domain size was determined based on a series of initial analyses where the load–displacement responses from models with the same anchor embedment depth but varying domain width were compared. The results of the sensitivity analysis revealed similar responses to some of the previous investigations reported by, for example, Chen *et al.* (2013). This sensitivity analysis has confirmed the adopted domain size to be adequate in eliminating any potential boundary effects. A zone with empty elements (void) was considered at the top of the domain to allow for a free movement of soil materials in the upward direction to capture a possible heave at the soil surface. The height of the void region was assumed as $2 \times B$. A representative finite-element mesh was used in the pull-out analysis and is shown in Fig. 1. A mesh sensitivity analysis was conducted wherein the minimum mesh size was varied between $B/20$ and $B/60$. The processing time for these analyses varied from 1·6 h to 66 h. The effect of using a mesh size of

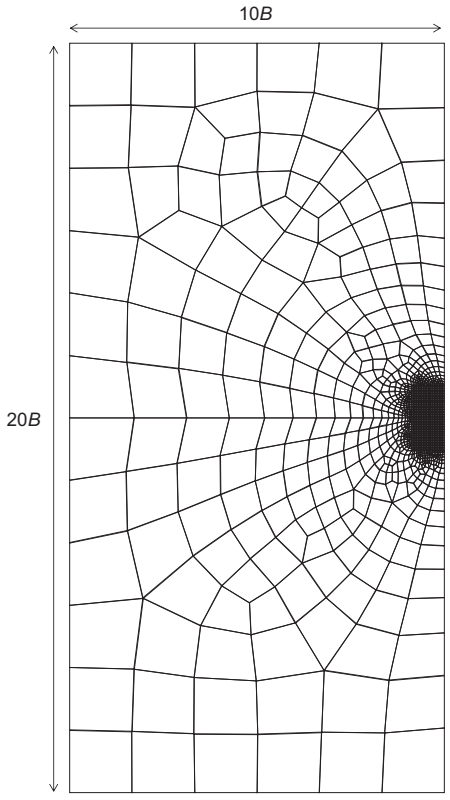

Fig. 1. Schematic diagram of finite-element model (top view)

B/40 instead of B/60 caused an error in predicting uplift capacity by 1% for a reduction of processing time from 66 h to 13·4 h. As a result, a minimum mesh size of B/40 was adopted in the region at the vicinity of the anchor. The influence of loading rate on the pseudo-static analysis was examined for the square plate anchor to obtain an optimum rate of loading at which convergence in the resulting pull-out capacities can be obtained at a reasonable computation cost. The loading rate was reduced from 0·32B/s to 0·005B/s. It was found that a loading rate of 0·02B/s yielded a result within 1% of that obtained using 0·005B/s. Therefore, a loading rate of 0·02B/s was adopted for the analyses reported herein (i.e. 20 mm/s for a square plate anchor of width (B) of 1 m).

RESULTS AND DISCUSSION

A series of pull-out tests on a square plate anchor ($B = 1$ m) was performed considering a range of variables, including soil unit weight, embedment depths and the undrained shear strength, as outlined in the previous section 'Methodology'.

Peak pull-out capacity

As a first step in the analyses, the effect of overburden ratio ($\gamma' H/s_u$) on the peak pull-out capacity factor N_c was determined and the analyses are shown in Fig. 2 in the form adopted by Song *et al.* (2008) and others for a range of normalised embedment depths, The results are consistent with previous studies undertaken using large-deformation finite-element analysis (Wang *et al.*, 2010; Chen *et al.*, 2013).

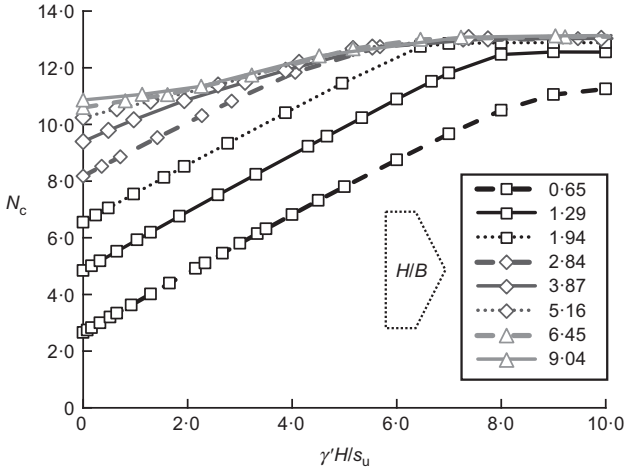

Fig. 2. Variation in pull-out capacity with overburden ratio and anchor embedment ratio

While the pull-out capacity is an important indicator of the ultimate performance of the anchor, a complete insight into the failure mechanism of an anchor cannot be established through the study of the pull-out capacity alone. In particular, the association of the specified failure modes to different soil strength ratios and anchor embedment depths (and the transition of failure mechanisms as a result of change in these parameters) is not readily established in the context of the pull-out capacity curves. In the subsequent sections the following aspects are further examined: (*a*) the anchor displacement required to mobilise the pull-out capacity; (*b*) the energy absorbed by the anchor during pull-out; and (*c*) the local slope of pull-out capacity curves on the failure mechanism developed by anchors during pull-out.

Pull-out displacement

This section examines the effect of anchor displacement on the mobilised pull-out capacity and associated failure mechanisms that can develop for a plate anchor, depending on the normalised depth and overburden ratios. To this end, a series of analyses for a square anchor plate ($B = 1$ m) in a weightless soil was performed ($\gamma' H/s_u = 0$). The data are provided in Fig. 3(a), which shows the variation in continuous pull-out force with increasing pull-out displacement at different H/B values. The displacement, w_p, corresponding to the peak pull-out force at each embedment depth is identified with square data points. It is clear that the normalised peak pull-out forces (N_{c0}) initially increased rapidly with embedment depth (H/B) while the peak pull-out displacements (w_p) increased only slightly. However, at large embedment ratios the N_{c0} values slowly converge to an upper limit while the corresponding w_p values increase much more rapidly. This is shown in Fig. 3(b) where super-linear and sub-linear rates of growth with embedment ratio (H/B) are observed for values of N_{c0} and w_p, respectively ($H/B < 9{\cdot}0$).

Figure 3 demonstrates a distinctive trend between the anchor pull-out capacity and displacement phenomena. However, the assessment is limited to an idealised case of a weightless soil ($\gamma' H/s_u = 0$) and it only considers the interaction between the load and displacement at the peak reaction stage. A more detailed assessment is shown in Fig. 4,

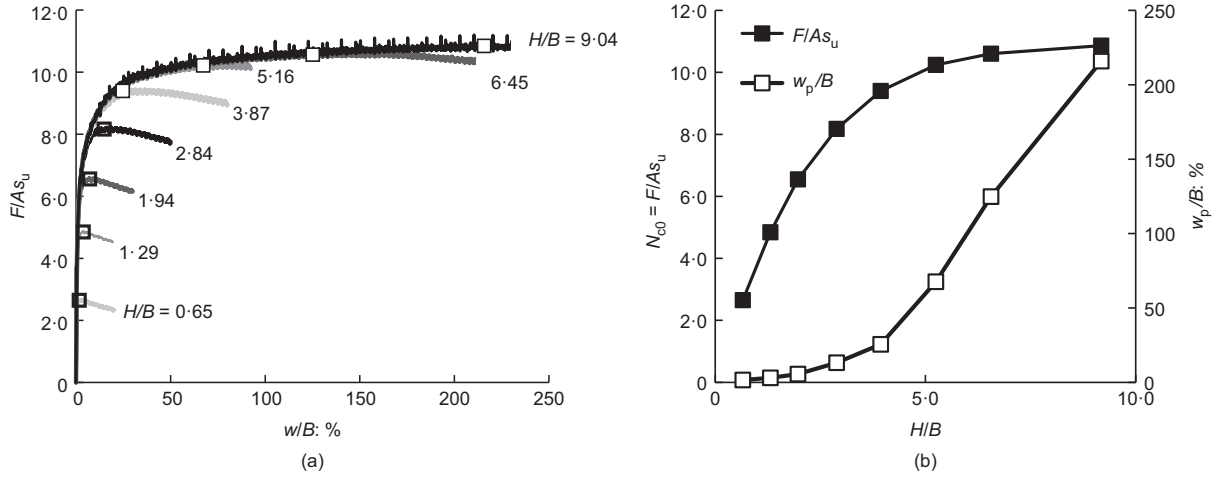

Fig. 3. (a) Variation in continuous pull-out force with increasing displacement of the plate (square symbol represents displacement, w_p, to peak capacity); (b) variation of peak pull-out force and associated displacement for anchor with different embedment ratios in weightless soil ($\gamma' H/s_u = 0$)

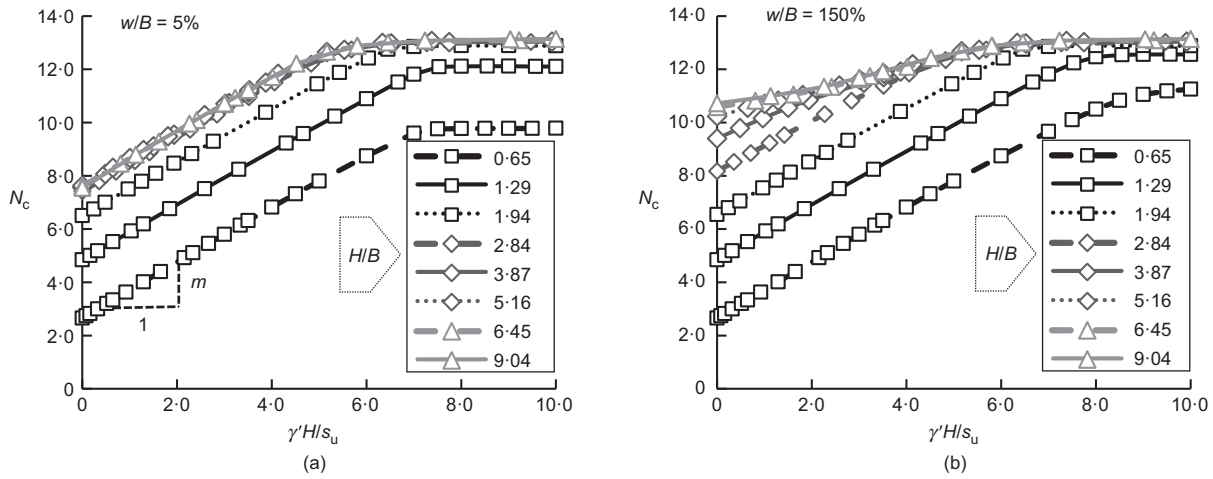

Fig. 4. Pull-out capacity at (a) 5% and (b) 150% normalised displacements

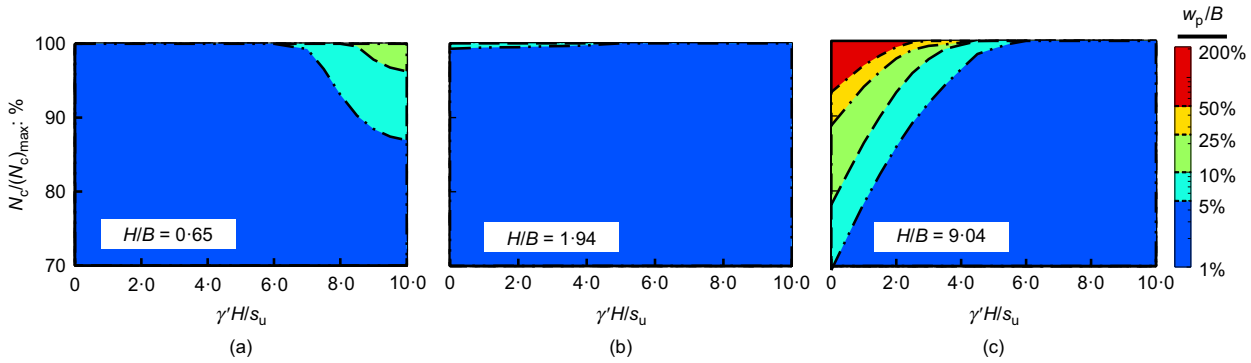

Fig. 5. The effect of normalised anchor depth, H/B, of (a) 0·65; (b) 1·94 and (c) 9·04 on the proportion of peak pull-out capacity mobilised at different displacement levels

where the correlation between the pull-out capacity and the displacement is demonstrated as a function of overburden ratios for a range of normalised displacements between 5% and 150%. The following trends are observed.

(*a*) At low overburden ratios ($\gamma' H/s_u < 5$)
  (*i*) at a low displacement level of 5% (Fig. 4(a)) the pull-out capacity curves converge for H/B values above 1·94 (i.e. pull-out capacity does not increase with depth), and the local slope, m_t is unity for all embedment depths
  (*ii*) as the displacement level increases (Fig. 4(b)) the pull-out capacity curves (for H/B values above 1·94) are observed to separate and the local slope m_t, reduces below unity with increase in depth.

(*b*) At high overburden ratios ($\gamma' H/s_u > 7$), increasing the displacement level above 5% results in a notable increase in the pull-out capacity of shallow anchors ($H/B < 2$), while the impact on deeper anchors is negligible.

(*c*) At intermediate overburden ratios ($5 < \gamma' H/s_u < 7$), the impact of displacement on the pull-out capacity of anchors with different embedment ratios is not significant.

The percentage of the peak pull-out capacity mobilised up to different levels of normalised displacement is shown in Fig. 5. Fig. 5(a) shows the typical responses of the anchors with $H/B < 2$, where displacements up to $w/B = 25\%$ are required to fully mobilise the capacity of anchors with large overburden ratios ($\gamma' H/s_u > 7$). Fig. 5(c) shows the typical responses of the anchors with $H/B > 2$, where displacements up to $w/B = 200\%$ are required to mobilise the capacity of anchors with small overburden ratios ($\gamma' H/s_u < 5$). Fig. 5(b) shows a transitional embedment depth ($H/B \cong 2$) where the capacity is fully mobilised at $w/B = 5\%$ for all overburden ratios considered.

A summary of the effect of normalised depth and overburden ratio on the displacement required to achieve the peak pull-out capacity is provided in Fig. 6. Two distinct regions can be identified, as described below.

(*a*) Regions where the peak pull-out capacity is mobilised at small displacements ($w/B = 5\%$ indicated by blue shading) are associated with the development of either a shallow or deep anchor failure mechanism. This region includes anchors with embedment depth $H/B < 2$ with overburden ratios of $\gamma' H/s_u < 7$, together with deeply embedded anchors ($H/B > 2$) with overburden ratios in excess of $\gamma' H/s_u = 5$. The curve for an anchor with a normalised embedment depth $H/B = 1{\cdot}94$ is the only one that falls almost entirely within the region where the pull-out capacity is fully developed at $w/B = 5\%$ for the entire range of overburden ratios considered.

(*b*) Regions of Fig. 6 where displacements in the range $w/B = 5\%$ and $w/B = 150\%$ are shown to be necessary to mobilise the peak capacity are indicative of the intermediate failure mechanism (Chen *et al.*, 2013). This occurs both at low and high overburden ratios. At low overburden ratios, deeper anchors ($H/B > 1{\cdot}9$) cannot develop a full-flow (deep) failure mechanism, as the overburden stress ratio is not high enough to cause the cavity to collapse behind the plate. At higher overburden

ratios ($\gamma' H/s_u > 7$), shallow anchors ($H/B < 1{\cdot}3$) cannot develop a (shallow) failure mechanism, as the undrained shear strength is not high enough to stabilise the cavity behind the plate.

Energy absorbed during pull-out

Given that the intermediate failure mechanism was characterised by the development of large w_p values to mobilise the peak capacity, the normalised energy absorbed by the anchor during the pull-out process (calculated as the area beneath the normalised force times normalised displacement curve) could provide an indication of the possible failure mode, particularly a large absorbed energy value may be associated with the intermediate failure mechanism, while low absorbed energy values may be related to shallow or deep failure modes. The energy absorbed during quasi-static pull-out of the anchor for different combinations of embedment depths and overburden ratios is shown in Fig. 7(a) where it can be seen that

(*a*) for shallow embedment depths ($H/B < 1{\cdot}94$), the energy absorbed by the anchor increased as the normalised stress ratio increased (or the soil strength reduced)

(*b*) for the anchor at $H/B = 1{\cdot}94$, the energy absorbed by the anchor was approximately constant for all overburden ratios considered

(*c*) for anchors with $H/B > 1{\cdot}94$, the energy absorbed by the anchor decreased as the normalised stress ratio increased with the values tending to converge to a unique lower limit at overburden ratios of above 6.

Figure 7(a) confirms that plate anchors with shallow, intermediate or deep behaviour exhibit distinct trends in the dissipated energy: the shallow and intermediate anchor responses are identified with increasing and decreasing trends, respectively, while the deep anchor behaviour is attributed to a lower-limit horizontal asymptote. In addition, while anchors with $H/B > 3{\cdot}87$ exhibited a general trend for the dissipated energy to decrease with increasing overburden stress ratio, a local maximum can be observed in Fig. 7(a) at an overburden ratio of $\gamma' H/s_u \cong 3{\cdot}5$. As will be discussed later, this corresponds to a characteristic point in the capacity curves that marks the dominance of the full-flow over the partial-flow mechanism. This is marked in Fig. 2 with the point of convergence of pull-out capacity curves for deeply embedded anchors ($H/B > 3{\cdot}87$) on a back-bone curve.

Figure 7(b) shows the influence of the overburden stress ratio and embedment depths on the variation of the peak pull-out displacement (w_p). For an overburden ratio of zero (weightless soil), w_p increases as the normalised embedment depth increased. For the highest overburden ratio of 10, w_p reduced rapidly at shallow embedment ratio, converging to a horizontal asymptote at large embedment depths. The data indicate the existence of an intermediate embedment depth $H/B \cong 2$ for which the peak pull-out displacement is unique for the range of overburden ratios considered in the present study. This agrees with the observations obtained from Fig. 7(a) and is associated with the absence of an intermediate failure mechanism at a depth of $H/B \cong 2$. For anchors with $H/B < 2$ the intermediate failure mechanism (associated with large pull-out displacement or high absorbed energy) is observed at high overburden ratios. For anchors with $H/B > 2$ the intermediate failure mode governs the response at low overburden ratios (soils with high strength). At low overburden ratios, $H/B \cong 2$ marks the transition between shallow and intermediate failure mechanisms (with increasing embedment depth). At high overburden ratios, $H/B \cong 2$ characterises the transition between

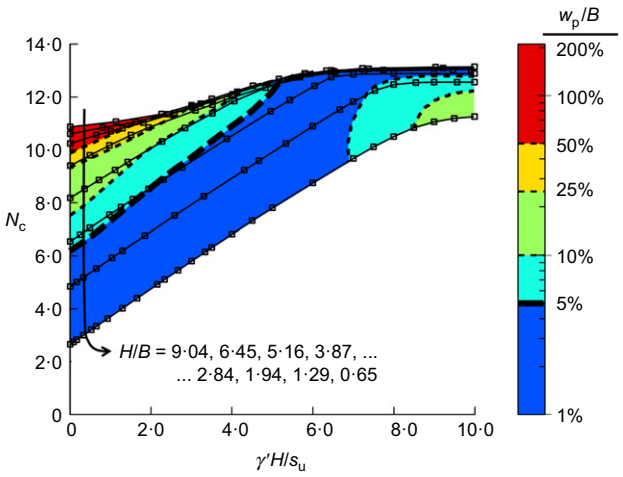

Fig. 6. The interaction of peak pull-out displacement and anchor capacity for various embedment depths and overburden ratios

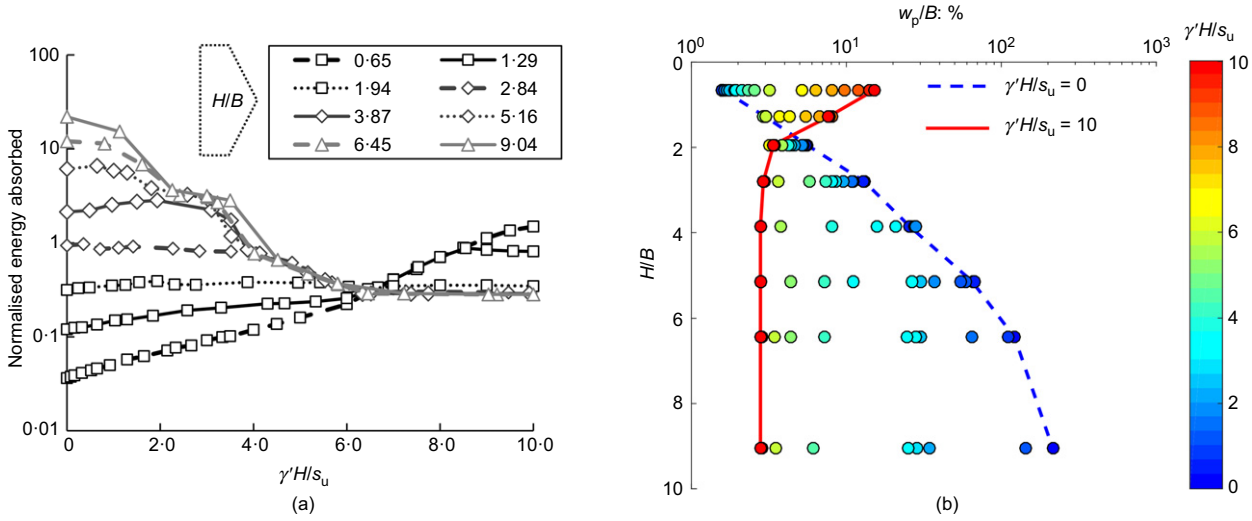

Fig. 7. (a) The normalised energy absorbed by the anchor during pull-out; (b) change in the pull-out displacement as a result of variation in overburden ratio

deep and intermediate failure mechanisms (with decreasing embedment depth).

Local slope of capacity diagrams (m_t)

As discussed earlier, in the bilinear form of pull-out capacity curves obtained by Merifield *et al.* (2003) using lower-bound analysis the local slope, m_t, is derived as 1·0 for shallow failure and zero for deep failure modes. However, consideration of large-deformation analysis by Wang *et al.* (2010), Chen *et al.* (2013) and the current study reveals that the local slope of capacity curves may vary between zero and 1·0 for anchors with large embedment depths and low overburden ratios where the intermediate failure mechanism dominates (see Fig. 2). To investigate the correlation between the anchor failure modes and the local slope of the pull-out capacity curve, at specific values of embedment depth and overburden ratio, a series of analyses was considered assuming the following two boundary conditions.

- Set 1 (BC-01): $\gamma' H/s_u = 0$ and $0{\cdot}65 < H/B < 9{\cdot}04$ – that is a weightless soil is modelled over the full range of anchor embedment depths.
- Set 2 (BC-02): $H/B = 9{\cdot}04$ and $0 < \gamma' H/s_u < 10$ – that is the deepest anchor was modelled over the full range of normalised stress ratios.

BC-01. Figure 8 shows the results obtained from the set 1 analysis, which also includes sub-illustrations showing the variation of the local slope m_t with H/B combined with schematics of the soil flow mechanism, at the point of failure for various embedment ratios along the curve. The peak pull-out displacement corresponding to anchor failure is denoted in each case as w_p/B. The flow mechanism represented in Fig. 8 is in terms of unit vectors and contours that demonstrate the direction ($\boldsymbol{v}/\|\boldsymbol{v}\|$) and magnitude ($\|\boldsymbol{v}\|$) of soil flow around the anchor, respectively. For the purpose of clarity, the points at which the magnitude of the flow is sufficiently small (less than 1/6 of the pull-out rate of the plate anchor) are excluded. The formation of a gap behind the plate anchor and the initial and final (at failure) embedment depths of the anchor are also indicated.

Based on the observations in Fig. 8, at shallow embedment depths ($H/B < 2$), a near-parallel and straight-sided failure surface develops. The displacements fully propagate to the soil surface and the peak pull-out capacity is mobilised at relatively low displacement ($w_p/B < 10\%$). The pull-out capacity for this shallow mode is governed by the shear stress that develops along the failure surfaces. For this case where the soil strength is uniform with depth, the pull-out capacity increases linearly with depth and $m_t = 1{\cdot}0$.

For H/B values in the range 2–3 the failure surface becomes more complex and w_p increases to up to 15%. Although surface displacements are still generated, the m_t value reduces below 1·0. As H/B increases, the failure surface becomes more localised around the anchor and w_p/B increases to 220% at $H/B = 9{\cdot}04$. It is evident that a full-flow failure mechanism does not develop, even for the deepest anchor ($H/B = 9{\cdot}04$) and the m_t value remains above 0.

BC-02. The variations in the bearing capacity factor N_c and the local slope (m_t) for a deeply embedded anchor ($H/B = 9{\cdot}04$) over a range of normalised stress ratios ($0 < \gamma' H/s_u < 10$) are shown in Fig. 9(a). The bearing capacity factor (solid line) increases from 10·9 (left-hand axis) to 13·1 as the normalised stress ratio (horizontal axis) increases. The local slope m_t (dashed line) increases from 0·15 (right-hand axis) at $\gamma' H/s_u = 0$ (horizontal axis) to a peak value of 0·5 at $\gamma' H/s_u = 3{\cdot}5$. The latter represents the inflection point on the pull-out capacity curve. As the overburden ratio increases, the local slope m_t reduces, converging to a lower-limit asymptote of zero. The peak pull-out displacement is shown in Fig. 9(b) where it is observed to consistently decrease from $w_p/B = 220\%$ at $\gamma' H/s_u = 0$ to less than 5% at $\gamma' H/s_u = 10$. A sudden drop in the values of peak pull-out displacement is identified at $\gamma' H/s_u = 3{\cdot}5$, which signals a transition in the anchor failure mechanism.

The evolution of the flow mechanisms corresponding to points A–F in Fig. 9(a), with respect to the level of pull-out displacement, is shown in Fig. 10. The final snapshot in each column shows the mechanism at the peak pull-out capacity. As before, the direction and magnitude of the flow are represented using a combination of unit vectors and

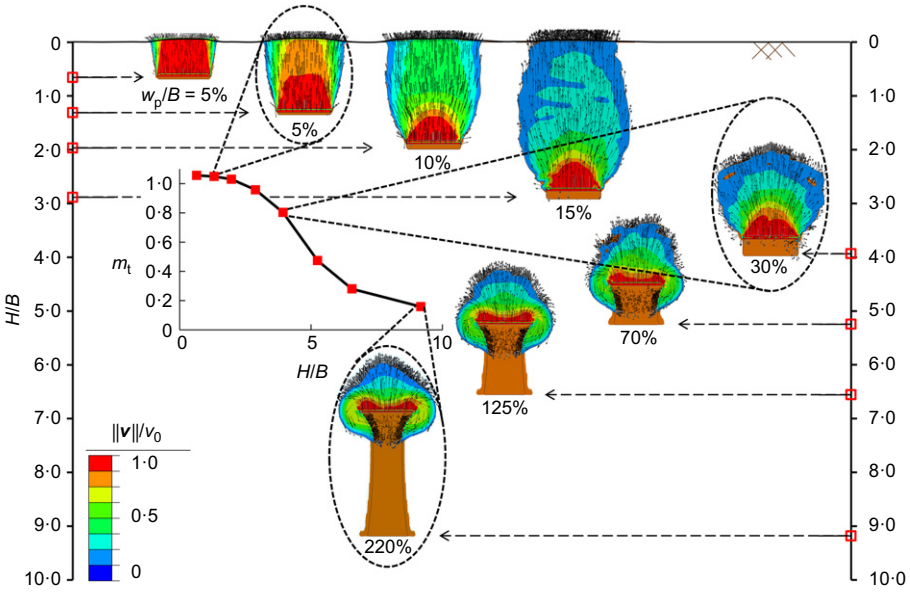

Fig. 8. Variation in the local slope, m_t with embedment depth obtained from the set 1 analysis. The flow velocity ($\|\boldsymbol{v}\|$) is normalised with respect to the pull-out rate of the anchor (v_0)

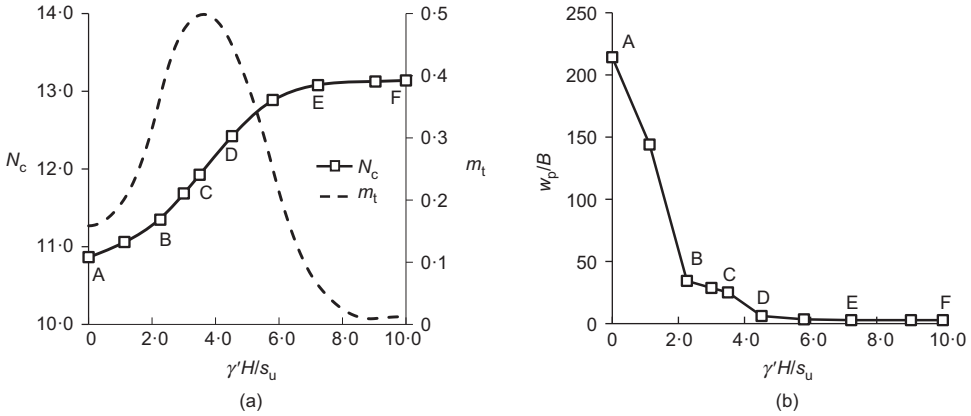

Fig. 9. (a) Variation in the local slope and (b) the peak pull-out displacement with overburden ratio obtained from the set 2 analysis

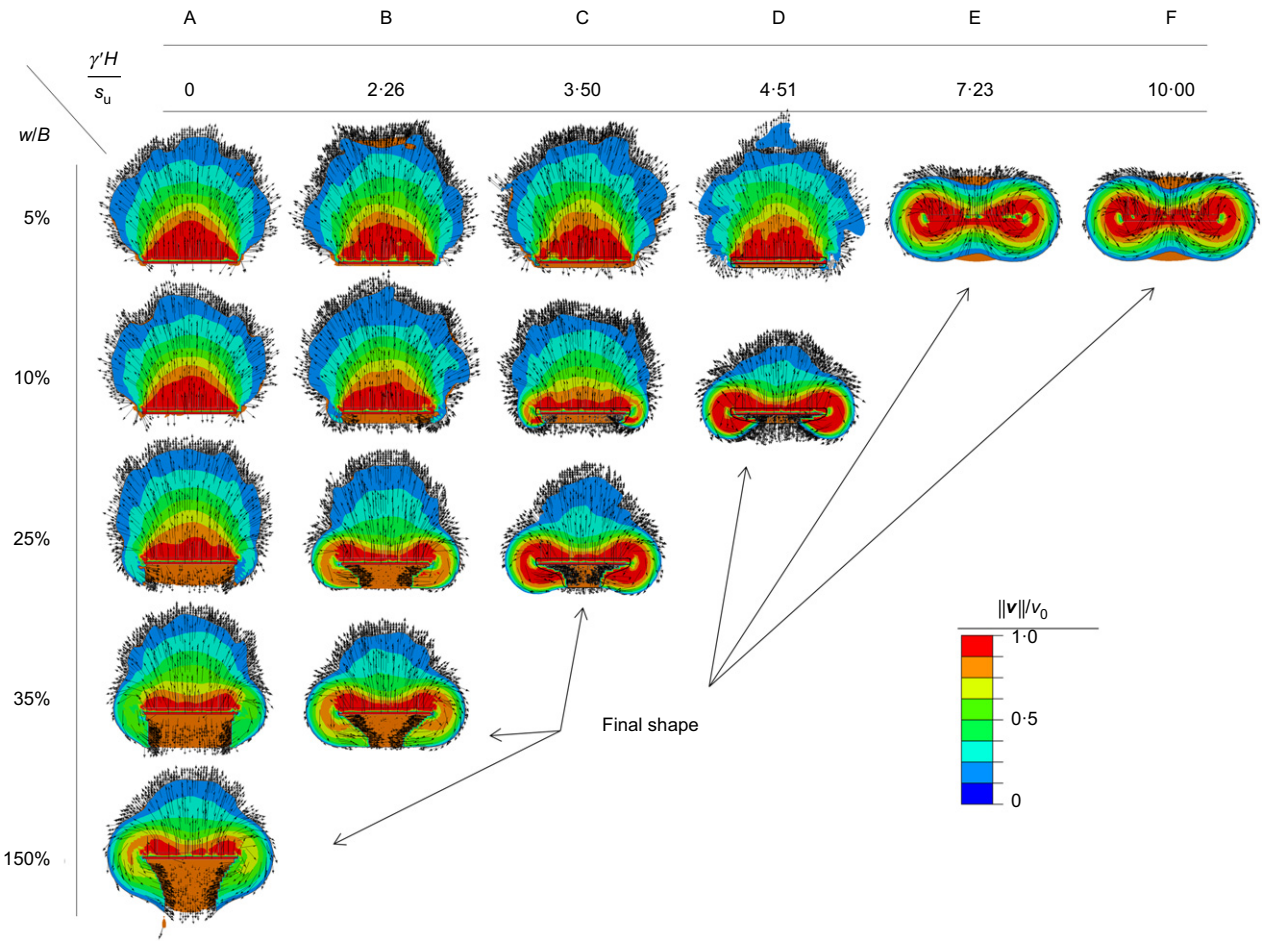

Fig. 10. The evolution of flow mechanism with pull-out displacement obtained from the set 2 analysis. The flow velocity ($\|v\|$) is normalised with respect to the pull-out rate of the anchor (v_0)

contours, respectively. The formation of the gap behind the anchor (and in its vicinity) is also depicted in Fig. 10.

The data show that, for a deeply embedded anchor, when the normalised stress ratio exceeded 7 (columns E and F in Fig. 10), a full-flow mechanism develops at relatively low displacement levels. For normalised stress levels less than 5, much larger displacements were required to mobilise the anchor capacity, with w_p increasing as the overburden stress ratio reduced. For these analyses (columns A–D) at low displacement levels, soil movements were predominantly vertically upwards – that is a shallow failure mechanism dominates. As the displacement level increased, partial flow around the anchor with gap closure occurs associated with the intermediate failure mechanism.

The inflection point of the capacity curve (the local peak in the m_t diagram in Fig. 9(a)) corresponds to an overburden ratio of 3·5 that divides the flow diagrams in Fig. 10 into two groups: the first corresponding to points A–C in Fig. 9 and columns A–C in Fig. 10, which exhibit large peak pull-out displacements, and the second, corresponding to points D–F in Fig. 9 (and columns D–F in Fig. 10) where failure develops at $w_p/B < 10\%$. It can be observed that for points on the right-hand side of the inflection point the flow of soil around the anchor is further inclined toward closure of the

gap behind the plate. Overall, it can be argued that a correlation exists between the inflection point on the m_t curve and the variation in anchor behaviour. In particular, the overburden ratio corresponding to the characteristic point represents the transition between intermediate and deep anchor response.

Combining all embedment depths and overburden ratios. The local slope, m_t, for a range of normalised anchor depths ($0{\cdot}65 < H/B < 9{\cdot}04$) and overburden stress ratios ($0 < \gamma' H/s_u < 10$), is presented in Fig. 11. As a reference, the data from Fig. 8 (set 1) represent the left-hand axis of Fig. 11, while Fig. 9(a) corresponds to the upper-bound N_c values for the range of overburden stress ratios considered (plotted on the x-axis). A notable feature of Fig. 11 is that the region on the plot where $m_t \approx 1{\cdot}0$ (shallow behaviour) spans a relatively wide range of normalised anchor depths and overburden ratios. Values of m_t below 1·0 and approaching zero (intermediate and deep behaviours) are confined to two key regions

(*a*) to the left-hand side of Fig. 11 where anchors with $H/B > 6{\cdot}45$ are embedded in soils with low overburden stress ratios (or high soil strength)
(*b*) a region to the right-hand side of Fig. 11 where anchors with $H/B > 1{\cdot}29$ are embedded in soil with $\gamma' H/s_u > 6$.

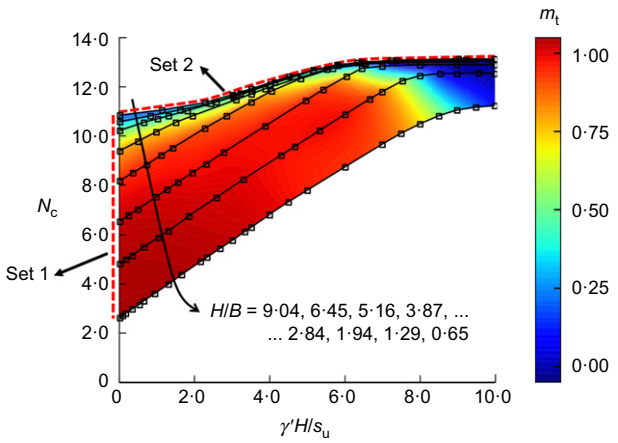

Fig. 11. Variation in the local slope (m_t), as a descriptor of anchor failure mode, with anchor embedment depth and overburden ratio

Areas where the local slope, m_t, approaches zero are confined to deeply embedded anchors ($H/B > 6{\cdot}5$) at very low normalised stress ratios and for all anchors in the region where the normalised stress ratio exceeds 8.

As both intermediate and deep anchor behaviours are represented with a common local slope value, the data in Fig. 11 are not sufficient for complete characterisation of anchor response. It is necessary that the findings from the study of local slope values m_t be viewed together with peak pull-out displacement data (Fig. 6) for a comprehensive understanding of anchor behaviour. This is demonstrated through consideration of boundary embedment depth and overburden ratio conditions summarised in Fig. 12. In particular, the shallow (Fig. 12(a)) and deep (Fig. 12(d)) anchor responses can be distinguished based on local slope values of close to 1 and zero, respectively. The deep anchor response (Fig. 12(d)) can be differentiated from intermediate behaviour (Fig. 12(c)) through the unambiguous peak pull-out displacement demonstrated by the latter (Fig. 6). In addition, the quasi-deep response experienced by shallow embedded anchors with large overburden ratios (Fig. 12(b)) that can be mistaken for a full flow in Fig. 11 (due to local slope values of close to zero), can correctly be distinguished in Fig. 6 through notably large peak displacement values.

SUMMARY DESIGN CHARTS

An important conclusion that can be drawn from this study is the dependence of pull-out capacity curves and, therefore, different parameters in equation (1), on the displacement level (see Fig. 6). This has practical implications in the design of

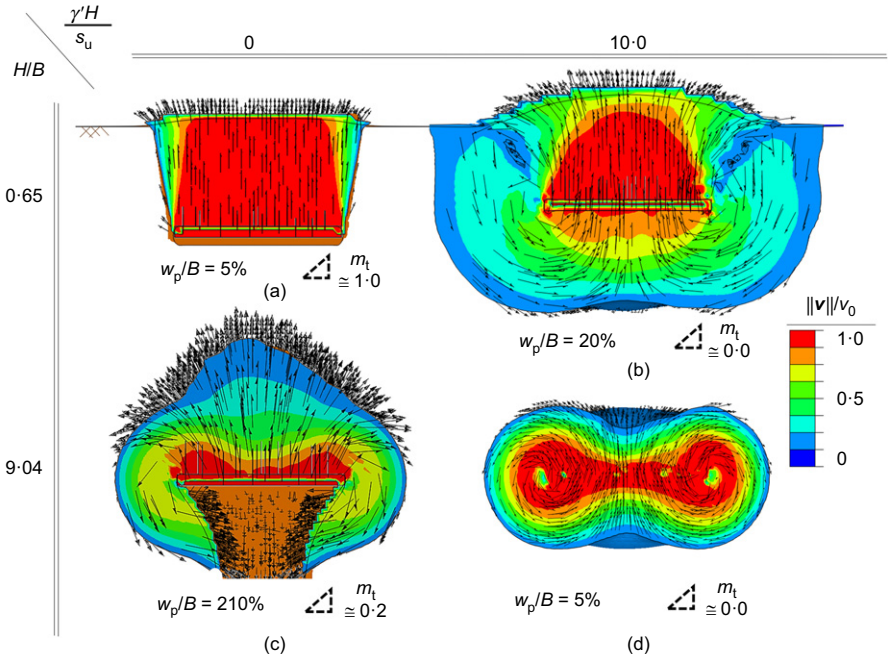

Fig. 12. Summary of flow mechanisms for (a) shallow; (b) quasi-deep; (c) intermediate and (d) deep anchor responses and distinction based on the peak pull-out displacement and the local slope (m_t)

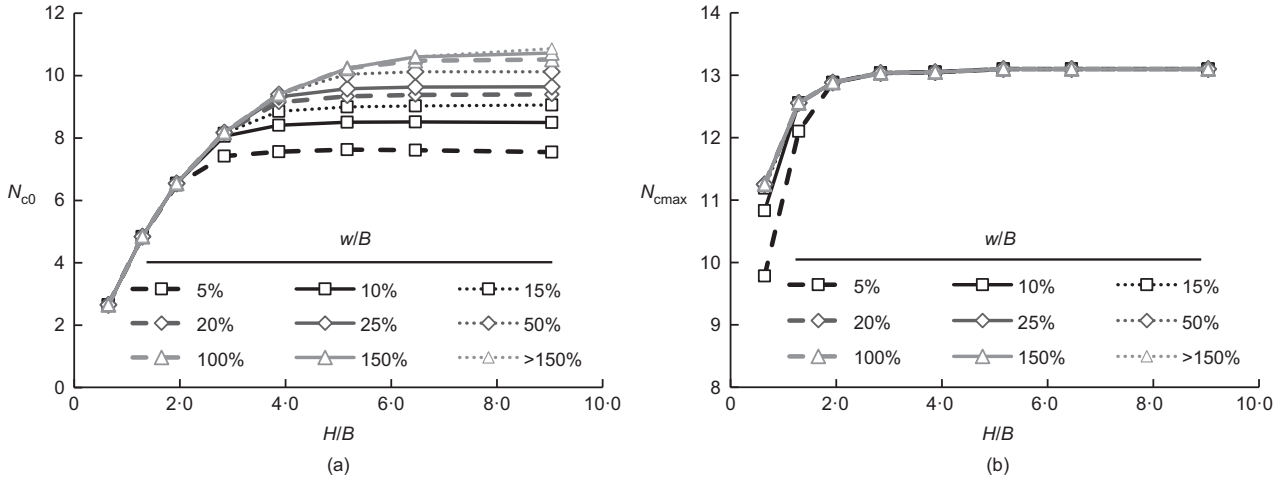

Fig. 13. Variation of (a) N_{c0} for weightless soil, and (b) $N_{c\,max}$, in equation (1) with embedment depth and displacement level

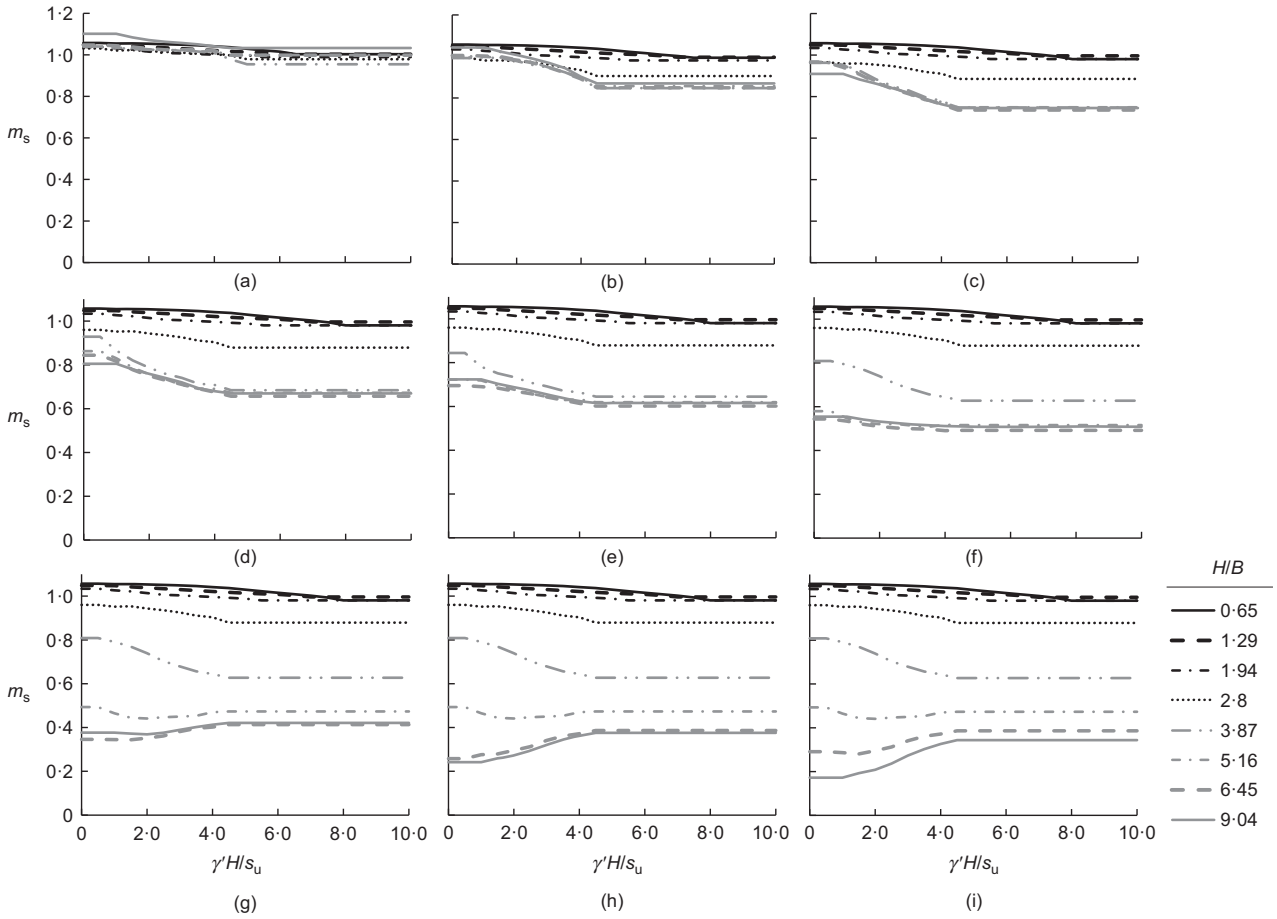

Fig. 14. Variation of design parameter, m_s, in equation (1), as a function of embedment depth, overburden ratio and pull-out displacement level: (a) $w/B = 5\%$; (b) $w/B = 10\%$; (c) $w/B = 15\%$; (d) $w/B = 20\%$; (e) $w/B = 25\%$; (f) $w/B = 50\%$; (g) $w/B = 100\%$; (h) $w/B = 150\%$; (i) $w/B = 210\%$;

pull-out capacity of vertical plate anchors, especially in scenarios where there is low tolerance on allowable displacement level due to serviceability requirements (e.g. for tension leg platforms). A quantitative assessment of different design parameters in equation (1) (i.e. N_{c0}, $N_{c\,max}$, m_s) as a function of embedment ratio, overburden ratio and pull-out displacement level is provided in Figs 13 and 14, which provides valuable insights for practical design purposes. It should be noted that these design charts are particularly relevant for typical soft marine deposits ($E/s_u \approx 500$) and further analyses are required for clay with higher stiffness.

CONCLUSIONS

The current study investigates the quasi-static pull-out behaviour of a square plate in a clay of uniform strength through an extensive series of large-deformation finite-element analyses. The plate anchor behaviour at various embedment depths (H) and overburden stress ratios ($\gamma' H/s_u$) in clay was examined. Three known regimes of anchor behaviour corresponding to shallow, intermediate and deep responses were evaluated in terms of (*a*) the pull-out capacity of the anchor, (*b*) the pull-out displacement, (*c*) the energy absorbed during pull-out and (*d*) the local slope of capacity curves.

Shallow and deep anchor mechanisms were seen to mobilise at low displacement levels. In contrast, large displacements were required to activate the intermediate failure mechanism. It was also shown that the shape of the capacity curve evolved during pull-out, as the displacement level increased. Simultaneous examination of the pull-out capacity and displacement was performed using the analysis of the energy absorbed by a plate anchor during pull-out. For the shallow mechanism the energy absorbed increased with increasing overburden ratio. In contrast the intermediate mechanism exhibited a decrease in energy absorbed. The deep anchor response was represented by a horizontal asymptote in the energy diagram. The study also confirmed the existence of an embedment depth that marked the transition between shallow and intermediate anchor behaviours at low overburden ratios, and intermediate and deep failure mechanisms at large overburden ratios.

The results allowed a correlation between the (local) slope of capacity curves and the respective anchor failure mechanisms to be developed. Both the shallow and the deep anchor response are identified by a characteristic local slope of unity and zero, respectively. The intermediate failure mechanisms are characterised by a local slope between unity and close to zero.

Design charts are presented that show the variation in different design parameters in equation (1) with anchor displacement level for the range of anchor embedment depth and overburden ratios considered in this study. These charts have practical design implications for anchors with low displacement tolerance in typical soft marine deposits ($E/s_u \approx 500$). Further work is underway to quantify the effect of rigidity index on the findings published in this paper.

ACKNOWLEDGEMENTS

This research was conducted with the financial support of Science Foundation Ireland under the US–Ireland R&D Partnership Programme grant number SFI/12/US/E2479, and National Science Foundation under grant no. 1300142. The authors wish to acknowledge the SFI/HEA Irish Centre for High-End Computing (ICHEC) for the provision of computational facilities and support.

NOTATION

A	bearing area of the anchor
B	width of the anchor
E	Young's modulus of the soil
F	pull-out force
H	embedded depth of the anchor
m_s	secant slope of the capacity curve
m_t	tangent slope of the capacity curve
N_c	pull-out capacity factor
N_{c0}	pull-out capacity factor in weightless soil
N_{cmax}	maximum pull-out capacity factor
s_u	undrained shear strength of the soil
$\|\|v\|\|$	flow velocity vector
v_0	pull-out velocity of the anchor
w	pull-out displacement
w_p	peak pull-out displacement
γ'	buoyant unit weight of the soil
ν	Poisson's ratio of the soil

REFERENCES

Aubeny, C. P. & Chi, C. (2010). Mechanics of drag embedment anchors in a soft seabed. *J. Geotech. Geoenviron. Engng* **136**, No. 1, 57–68.

Blake, A. P., O'Loughlin, C. D. & Gaudin, C. (2015). Capacity of dynamically embedded plate anchors as assessed through field tests. *Can. Geotech. J.* **52**, No. 1, 87–95.

Chen, Z., Tho, K. K., Leung, C. F. & Chow, Y. K. (2013). Influence of overburden pressure and soil rigidity on uplift behaviour of square plate anchor in uniform clay. *Comput. Geotech.* **52**, 71–81.

Das, B. M. (1980). A procedure for estimation of ultimate uplift capacity of foundations in clay. *Soils Found.* **20**, No. 1, 77–82.

Dutta, S., Hawlader, B. & Phillips, R. (2015). Finite element modeling of partially embedded pipelines in clay seabed using coupled Eulerian–Lagrangian method. *Can. Geotech. J.* **52**, No. 1, 58–72.

Fahmy, A. M., de Bruyn, J. R. & Newson, T. A. (2013). Numerical investigation of the inclined pull-out behaviour of anchors embedded in clay. *Geotech. Geol. Engng* **31**, No. 5, 1525–1542.

Fallah, S., Gavin, K. & Moradabadi, E. (2015). Estimation of spudcan penetration using a probabilistic Eulerian finite element analysis. In *Frontiers in offshore geotechnics III* (ed. V. Meyer), pp. 1281–1286. Boca Raton, FL, USA: CRC Press.

Gerkus, H. (2016). *Model experiments to measure yield thresholds and trajectories for plate anchors and develop a new anchor concept*. *Doctoral dissertation*, University of Texas at Austin, Austin, TX, USA.

Gilbert, R. B., Lupulescu, C., Lee, C. H., Miller, J., Kroncke, M., Yang, M., Aubeny, C. P. & Murff, J. D. (2009). Analytical and experimental modeling for out-of-plane loading of plate anchors. *Proceedings of the offshore technology conference*, Houston, TX, USA, paper OTC-20115-MS.

Hu, Y., Liu, J., Yu, L. & Kong, X. J. (2011). Numerical study on plate anchor stability in clay. *Géotechnique* **61**, No. 3, 235–246, https://doi.org/10.1680/geot.8.P.071.

Hu, P., Wang, D., Cassidy, M. J. & Stanier, S. A. (2014). Predicting the resistance profile of a spudcan penetrating sand overlying clay. *Can. Geotech. J.* **51**, No. 10, 1151–1164.

Hu, P., Wang, D., Stanier, S. A. & Cassidy, M. J. (2015). Assessing the punch-through hazard of a spudcan on sand overlying clay. *Géotechnique* **65**, No. 11, 883–896, https://doi.org/10.1680/jgeot.14.P.097.

Ko, J., Jeong, S. & Lee, J. K. (2016). Large deformation FE analysis of driven steel pipe piles with soil plugging. *Comput. Geotech.* **71**, 82–97.

Liu, H., Liu, C., Zhao, Y. & Wang, C. (2013). Reverse catenary equation of the embedded installation line and application to the kinematic model for drag anchors. *Appl. Ocean Res.* **43**, 80–87.

Merifield, R. S., Lyamin, A. V., Sloan, S. W. & Yu, H. S. (2003). Three-dimensional lower bound solutions for stability of plate anchors in clay. *J. Geotech. Geoenviron. Engng* **129**, No. 3, 243–253.

Merifield, R. S., Lyamin, A. V. & Sloan, S. W. (2005). Stability of inclined strip anchors in purely cohesive soil. *J. Geotech. Geoenviron. Engng* **131**, No. 6, 792–799.

Murff, J. D., Randolph, M. F., Elkhatib, S., Kolk, H. J., Ruinen, R., Strom, P. J. & Thorne, C. (2005). Vertically loaded plate anchors for deepwater applications. In *Frontiers in offshore geotechnics* (eds S. Gourvenec and D. Cassidy), pp. 31–48. Boca Raton, FL, USA: CRC Press.

O'Neill, M. P., Bransby, M. F. & Randolph, M. F. (2003). Drag anchor fluke–soil interaction in clays. *Can. Geotech. J.* **40**, No. 1, 78–94.

Pucker, T. & Grabe, J. (2012). Numerical simulation of the installation process of full displacement piles. *Comput. Geotech.* **45**, 93–106.

Qiu, G., Henke, S. & Grabe, J. (2011). Application of a coupled Eulerian-Lagrangian approach on geomechanical problems involving large deformations. *Comput. Geotech.* **38**, No. 1, 30–39.

Schwartz, M. N., Heimiller, D., Haymes, S. & Musial, W. (2010). *Assessment of offshore wind energy resources for the United States*, Technical Report NREL/TP-500-45889. Golden, CO, USA: National Renewable Energy Laboratory.

Shelton, J. T. (2007). OMNI-Maxtrade anchor development and technology. *Proceedings of OCEANS conference*, Vancouver, BC, Canada, https://doi.org/10.1109/OCEANS.2007.4449415.

Singh, S. P. & Ramaswamy, S. V. (2008). Effect of shape on holding capacity of plate anchors buried in soft soil. *Geomech. Geoengng* **3**, No. 2, 145–154.

Song, Z., Hu, Y. & Randolph, M. F. (2008). Numerical simulation of vertical pull-out of plate anchors in clay. *J. Geotech. Geoenviron. Engng* **134**, No. 6, 866–875.

Tho, K. K., Leung, C. F., Chow, Y. K. & Swaddiwudhipong, S. (2012). Eulerian finite-element technique for analysis of jack-up spudcan penetration. *Int. J. Geomech.* **12**, No. 1, 64–73.

Tho, K. K., Chen, Z., Leung, C. F. & Chow, Y. K. (2013). Pull-out behaviour of plate anchor in clay with linearly increasing strength. *Can. Geotech. J.* **51**, No. 1, 92–102.

Tolooiyan, A. & Gavin, K. (2011). Modelling the cone penetration test in sand using cavity expansion and arbitrary Lagrangian Eulerian finite element methods. *Comput. Geotech.* **38**, No. 4, 482–490.

Wang, D., Hu, Y. & Randolph, M. F. (2010). Three-dimensional large deformation finite-element analysis of plate anchors in uniform clay. *J. Geotech. Geoenviron. Engng* **136**, No. 2, 355–365.

Wang, D., Bienen, B., Nazem, M., Tian, Y., Zheng, J., Pucker, T. & Randolph, M. F. (2015). Large deformation finite element analyses in geotechnical engineering. *Comput. Geotech.* **65**, 104–114.

Wong, P., Gaudin, C., Randolph, M. F., Cassidy, M. J. & Tian, Y. (2012). Performance of suction embedded plate anchors in permanent mooring applications. In *Proceedings of the 22nd international offshore and polar engineering conference, Rhodes, Greece*, pp. 640–645. Cupertino, CA, USA: International Society of Offshore and Polar Engineers.

Yang, M., Murff, J. D. & Aubeny, C. P. (2010). Undrained capacity of plate anchors under general loading. *J. Geotech. Geoenviron. Engng.* **136**, No. 10, 1383–1393.

Yu, L., Liu, J., Kong, X. & Hu, Y. (2009). Three-dimensional numerical analysis of the keying of vertically installed plate anchors in clay. *Comput. Geotech.* **36**, No. 4, 558–567.

Zhao, Y. & Liu, H. (2016). Numerical implementation of the installation/mooring line and application to analyzing comprehensive anchor behaviours. *Appl. Ocean Res.* **54**, 101–114.